



Representation of stress tensor perturbations with application in machine-learning-assisted turbulence modeling

Jin-Long Wu^a, Rui Sun^a, Sylvain Laizet^b, Heng Xiao^{a,*}

^a Department of Aerospace and Ocean Engineering, Virginia Tech, Blacksburg, VA 24060, United States

^b Department of Aeronautics, Imperial College London, London, United Kingdom

Received 6 June 2018; received in revised form 30 August 2018; accepted 4 September 2018

Available online 27 September 2018

Abstract

Numerical simulations based on Reynolds-Averaged Navier–Stokes (RANS) equations are widely used in engineering design and analysis involving turbulent flows. However, RANS simulations are known to be unreliable in many flows of engineering relevance, which is largely caused by model-form uncertainties associated with the Reynolds stresses. Recently, a machine-learning approach has been proposed to quantify the discrepancies between RANS modeled Reynolds stress and the true Reynolds stress. However, it remains a challenge to represent discrepancies in the Reynolds stress eigenvectors in machine learning due to the requirements of spatial smoothness, frame-independence, and realizability. This challenge also exists in the data-driven computational mechanics in general where quantifying the perturbation of stress tensors is needed. In this work, we propose three schemes for representing perturbations to the eigenvectors of RANS modeled Reynolds stresses: (1) discrepancy-based Euler angles, (2) direct-rotation-based Euler angles, and (3) unit quaternions. We compare these metrics by performing *a priori* and *a posteriori* tests on two canonical flows: fully developed turbulent flows in a square duct and massively separated flows over periodic hills. The results demonstrate that the direct-rotation-based Euler angles representation lacks spatial smoothness while the discrepancy-based Euler angles representation lacks frame-independence, making them unsuitable for being used in machine-learning-assisted turbulence modeling. In contrast, the representation based on unit quaternion satisfies all the requirements stated above, and thus it is an ideal choice in representing the perturbations associated with the eigenvectors of Reynolds stress tensors. This finding has clear importance for uncertainty quantification and machine learning in turbulence modeling and for data-driven computational mechanics in general.

© 2018 Elsevier B.V. All rights reserved.

Keywords: Machine learning; Turbulence modeling; Unit quaternion; Euler angles

Notation

We summarize the notations to illustrate the convention of the nomenclature used in this paper. Upper case letters (e.g., \mathbf{Q}) indicate matrices or tensors; lower case letters with bold font (e.g., \mathbf{n}) indicate vectors; undecorated letters

* Corresponding author.

E-mail addresses: jinlong@vt.edu (J.-L. Wu), hengxiao@vt.edu (H. Xiao).

in lower cases indicate scalars. Tensors (matrices) and vectors are also indicated with index notations, e.g., R_{ij} and u_i with $i, j = 1, 2, 3$. In this paper, i and j are used with tensor indexes while α is used as general indexes. The ensemble average is indicated by $\bar{\square}$. The superscript \square^o denotes original quantities given by the Reynolds-Averaged Navier–Stokes simulations (baseline for the perturbations), and the superscript \square^* represents the truth or the target of perturbations. A list of nomenclature is presented in [Appendix](#).

1. Introduction

1.1. Challenges and new developments in turbulence modeling

Numerical simulations based on Reynolds-Averaged Navier–Stokes (RANS) equations are still the dominant tool for industry applications involving turbulent flows, even though the rapid growth of computational resource has greatly expanded the reach of the high-fidelity simulation methods such as Direct Numerical Simulation (DNS) and Large Eddy Simulation (LES) in the past few decades. However, commonly used RANS models (e.g., k - ε models, k - ω models and S–A models) are known to be unreliable in many flows such as those with three-dimensional separations, strong pressure gradients or mean streamline curvature [1]. This lack of accuracy mainly originates from a large discrepancy between the modeled and the true Reynolds stresses, leading to the unreliable predictions of other quantities of interests (QoIs) such as mean velocity, mean pressure, surface friction, and drag and lift forces.

In light of the decades-long stagnation in traditional RANS modeling, several researchers developed machine-learning-assisted turbulence models [2–4]. These efforts aimed at leveraging machine learning algorithms and large amounts of data made available by advances in experimental techniques and computational sciences. Duraisamy and co-workers [4,5] identified the target of machine-learning-assisted models as the multiplicative discrepancy in the production term of the transport equations of turbulent quantities (e.g., \tilde{v}_t in the S–A model). Although recent studies showed the potential of extrapolation capabilities of this approach among different flows [4,6], such capabilities are potentially limited by the lack of physical anchoring and uniqueness of the multiplicative discrepancy term. On the other hand, Ling et al. [3] incorporated physical knowledge in designing the architecture of a machine-learning-assisted model by adopting an invariant-set-based representation of Reynolds stress anisotropy tensor [7]. Their approach has clear physical justification, but note that their aim was to replace the traditional turbulence models with a data-driven, machine-learning-based counterpart. Xiao and co-workers [2,8] argued that data-driven models should be used to assist and complement, rather than replace, the traditional turbulence models. They justified their philosophical argument with the fact that currently used turbulence models condensed a lot of physical and theoretical insights, which in turn were distilled from large amounts of data and empirical knowledge in decades of engineering practice. In addition, these models have achieved great successes in engineering turbulent flow simulations despite the above-mentioned limitations. As such, Wang et al. [2] proposed a machine-learning-assisted turbulence modeling framework, where they identified the perturbations that can correct RANS-modeled Reynolds stresses to the true Reynolds stress as the target of learning. While this work focuses on RANS modeling, we note that several data-driven approaches have also been proposed in the context of LES to improve sub-grid scale stress models [9] and scalar fluxes models [9,10].

1.2. Stress perturbations in machine-learning-assisted RANS modeling

Wang et al. [2] represented the perturbations to RANS modeled Reynolds stress by following the decomposition method of Iaccarino and co-workers in their model-form uncertainty quantification work [11–13]. Emory et al. [11] decomposed the Reynolds stress anisotropic tensor into eigenvalues and eigenvectors, and then they used Barycentric triangle to provide a realizability map for the eigenvalues. The Barycentric triangle is equivalent to the well-known Lumley triangle [14,15]. These two equivalent maps provide a convenient way to ensure the realizability of the perturbed Reynolds stresses by bounding the mapped eigenvalues within the respective triangles. The theoretical foundation is that, after the corresponding transformations [14], a Reynolds stress tensor must reside within or on the edge of the Lumley or Barycentric triangle. However, much less work has been devoted to representing the perturbations to the eigenvectors of the RANS modeled Reynolds stress tensor.

Perturbations to eigenvectors are much more difficult to impose compared with that to the eigenvalues, which is due to several reasons. First, there is no straightforward bound on eigenvector perturbations — Reynolds stress realizability as represented by the Barycentric triangle only provides a bound for the eigenvalues and not for the eigenvectors. In

the context of uncertainty estimation, researchers investigated several representations of eigenvector perturbations. Thompson et al. [16] used the Reynolds stress transport equations to constrain the eigenvector perturbations based on the bounds on the eigenvalue perturbations. Their work can potentially address the challenge of bounding eigenvector perturbations. However, it should be noted that the Reynolds stress transport equations have several unclosed source terms (e.g., pressure-strain tensor, triple correlation) that must be estimated, which makes the transport-equation-based constraint a soft rather than a strict one. On the other hand, Iaccarino et al. [17] proposed an approach to augment their eigenvalue perturbations by using the maximum and minimum of turbulence production as bounds for perturbing the eigenvectors. Such bounds are physically sound, albeit not necessarily as mathematically rigorous as that in [16]. In addition to the lack of straightforward bounds, another challenge is that any perturbations introduced to the eigenvectors must retain their orthonormality. This is to ensure the symmetry and realizability of the perturbed Reynolds stress tensor. Such a requirement immediately rules out the option of introducing componentwise discrepancy tensor to eigenvectors or to the Reynolds stress tensor itself. Instead, a straightforward method to retain such orthonormality is to represent the eigenvector perturbations as a three-dimensional rigid-body rotation. In this spirit, Wang et al. [18] introduced such perturbations to the eigenvectors by using Euler angles for quantifying RANS model-form uncertainties [18].

The work reviewed above on introducing perturbations to modeled Reynolds stresses are all concerned with RANS model-form uncertainty estimations. A closely related topic is machine-learning-assisted turbulence modeling as in the framework of [2], where the objective is to predict the perturbations $\Delta\mathbf{R}$ needed to correct the modeled Reynolds stresses \mathbf{R}^{rans} to the true \mathbf{R}^* . They used machine learning to train a function $f : \mathbf{q} \mapsto \Delta\mathbf{R}$ between mean flow features \mathbf{q} and Reynolds stress perturbations $\Delta\mathbf{R}$. It should be noted that a general functional form $f : \mathbf{q} \mapsto \Delta\mathbf{R}$ is trained to map the mean flow features \mathbf{q} at any given location of the training flows to the corresponding Reynolds stress discrepancy $\Delta\mathbf{R}$. By doing so, the machine learning trained function f carries no information of the geometry of the training flows, which enables the prediction of the flow with different geometry configurations. By correcting the RANS-predicted Reynolds stresses towards the DNS counterparts, such perturbations are expected to improve the predictions of the velocity field and other quantities of interest. Wang et al. [2] used the random forest to learn such perturbations from a database of training flows with DNS data. In that work, the fully developed turbulent flow in a square duct and the flow over periodic hills were first studied to demonstrate the merit of modeling Reynolds stress by using machine learning. In a following report of Wang et al. [19], they further demonstrated the improvement of mean velocity prediction. The more general philosophy of machine-learning-assisted turbulence modeling was discussed in [8,20]. Recently, Wu et al. [21] proposed a stabilized machine learning scheme for RANS modeling and demonstrated better predictive capability of mean velocity. Wu et al. [22] further demonstrated that the performance of the machine-learning-assisted model depends on the choice of training flows by studying a group of flows with massive separation. In addition, Wu et al. [22] proposed two statistical metrics to assess the prediction performance *a priori* by evaluating the difference between the training flow and the test flow. In the context of machine-learning-assisted RANS modeling, the bounds for the eigenvectors perturbations are not required explicitly; instead, the main concern is to ensure the orthonormality of the machine-learning-corrected Reynolds stress eigenvectors. To this end, they used Euler angles to represent the eigenvectors perturbations as rigid-body rotations following the work by Wang et al. [18]. In fact, the representation of rigid-body rotation has attracted much more attention in robotics and computer vision [23], where different approaches including those based on Euler angles [24], unit quaternion [25] and rotation matrices of direction-cosines [26] have been evaluated and compared.

However, the usages of the above approaches to represent the eigenvectors perturbations to Reynolds stress tensors pose unique requirements in the context of machine-learning-assisted modeling. In particular, the functional form $f : \mathbf{q} \mapsto \Delta\mathbf{R}$ between mean flow features and desired Reynolds stress perturbations should be smooth to ensure that f can be learned from data [27]. Otherwise, the machine learning algorithms tend to fit the noise rather than the true functional relation. Another requirement is the frame-independence of the representation of Reynolds stress perturbations. In this work, we first address the smoothness requirement by comparing three representations of eigenvectors perturbations via *a priori* tests in Section 4.2. We then evaluate the performances of Euler angles and unit quaternion in the context of the machine-learning-assisted turbulence modeling in Section 4.3.

1.3. Novelty and potential impact of present work

The novelty of the present contribution is twofold. First, we explored several alternatives in representing the perturbations on Reynolds stress eigenvectors as rigid-body rotations, which ensure the orthonormality of the

perturbed eigenvectors by construction and thus the symmetry and positive definiteness (realizability) of the perturbed Reynolds stresses. Second, we performed a comprehensive comparison of two types of representation of rigid-body rotations, Euler angles and unit quaternions, in light of the two requirements posed by machine-learning-assisted turbulence modeling, i.e., smoothness and frame-independence. The assessment demonstrates that the unit-quaternion-based representation satisfies both requirements, making it superior to Euler-angle-based representations of eigenvectors perturbation for machine-learning-assisted turbulence modeling. As the machine learning techniques have gained increasing interests in turbulence modeling, the present manuscript deals with one of the most important aspects, i.e., to incorporate the physical constraints into machine-learning-based computational physics. Specifically, the objectivity requirement of the model is ensured by properly choosing the inputs and outputs of machine learning. The authors hope that the attempt of this work can inspire more turbulence modeling researchers to incorporate their domain knowledge of flow physics into machine-learning-assisted modeling.

Although this work mainly focus on the representation of Reynolds stress perturbations for machine-learning-assisted turbulence modeling, it is also applicable to the modeling of stress tensor field in general and thus has following potential broader impact in other research areas:

1. The objectivity (frame-independence) requirement is also important for machine-learning-assisted physics modeling in general and this work illustrated one possibility to satisfy such a requirement by properly choosing the outputs of machine learning in our framework.
2. We highlighted the smoothness requirements for machine-learning-assisted physics modeling where a spatial field needs to be predicted. Such highlighted requirement is also of importance in the model-form uncertainty quantification of the stress tensor field, particularly for the uncertainty quantification for the orientation of the modeled stress tensor.
3. The representation of perturbations on Reynolds stress tensors is directly applicable in other fields of computational mechanics, e.g., plasticity, where sequential increments of stress tensors are used to find a path from the current stress state to the new state.

The rest of the paper is organized as follows. Section 2 summarizes the machine-learning-assisted turbulence modeling framework of Wang et al. [2]. Section 3 introduces three representations of the eigenvectors perturbations to the Reynolds stress tensor, including direct-rotation-based Euler angles, discrepancy-based Euler angles, and the unit quaternion. Section 4 presents the results in evaluating these three representations of eigenvectors perturbations. Finally, Section 5 presents the conclusions.

2. Summary of machine-learning-assisted turbulence modeling framework

2.1. Origin of RANS model-form uncertainty

The Navier–Stokes (NS) equations for incompressible flows with a constant density ρ can be written as follows:

$$\frac{\partial u_i}{\partial t} + \frac{\partial (u_i u_j)}{\partial x_j} = -\frac{1}{\rho} \frac{\partial p}{\partial x_i} + \nu \frac{\partial^2 u_i}{\partial x_j \partial x_j} \quad (1a)$$

$$\text{and } \frac{\partial u_i}{\partial x_i} = 0 \quad (1b)$$

where u_i and p are instantaneous velocity and pressure, respectively; t and x_i are time and space coordinates, respectively; ν is the kinematic viscosity. Solving the Navier–Stokes equations directly would necessitate resolving a wide range of spatial and temporal scales, which would incur prohibitive computational costs. Therefore, when simulating turbulent flows in engineering, the instantaneous fields u_i and p in the NS equations are usually decomposed into their means (\bar{u}_i and \bar{p} , respectively) and the fluctuations (u'_i and p') around the means, i.e.,

$$u_i = \bar{u}_i + u'_i \quad (2)$$

$$p = \bar{p} + p' \quad (3)$$

Substituting the Reynolds decomposition above into the NS equation yields the RANS equations, which describe the mean velocities and pressure:

$$\frac{\partial \bar{u}_i}{\partial t} + \frac{\partial (\bar{u}_i \bar{u}_j)}{\partial x_j} = -\frac{1}{\rho} \frac{\partial \bar{p}}{\partial x_i} + \nu \frac{\partial^2 \bar{u}_i}{\partial x_j \partial x_j} - \frac{\partial \langle u'_i u'_j \rangle}{\partial x_j} \tag{4a}$$

$$\text{and } \frac{\partial \bar{u}_i}{\partial x_i} = 0 \tag{4b}$$

where negative of the velocity fluctuation covariance $\langle u'_i u'_j \rangle$ is referred to as Reynolds stress and is denoted as R_{ij} or \mathbf{R} for simplicity. It is a consensus that in incompressible, fully turbulent flows (i.e., flows without transition, heat transfer, or compressible effects), the modeled Reynolds stress term is the main source of model-form uncertainties in RANS simulations [7,28]. At any point in the flow field, the true Reynolds stress \mathbf{R}^* can be written as the sum of the RANS-modeled value and a discrepancy term, i.e., $\mathbf{R}^* = \mathbf{R}^{rans} + \Delta\mathbf{R}$. Aiming at estimating the Reynolds stress discrepancy $\Delta\mathbf{R}$, Wang et al. [2] proposed a machine-learning-assisted turbulence modeling framework, which is detailed below.

2.2. Machine-learning-assisted turbulence modeling framework

The essence of the machine-learning-assisted turbulence modeling framework of Wang et al. [2] is to predict the discrepancy term $\Delta\mathbf{R}$ by learning a model from high-fidelity simulation (e.g., DNS) data. This is achieved by learning a functional mapping $f : \mathbf{q} \mapsto \Delta\mathbf{R}$, where \mathbf{q} indicates mean flow features obtained from RANS simulations, e.g., mean pressure gradient, mean flow curvature, all normalized with local quantities. In machine learning terminology the discrepancy $\Delta\mathbf{R}$ is referred to as *responses*, the feature vector \mathbf{q} as the *inputs*, and the mappings f as *regression functions*. The flows used to train the *regression functions* are referred to as *training flows*, and the flow to be predicted as *test flow*. Random forest regression is used to build the regression functions. An advantage of the random forest regressor is that importance scores are also provided for each input flow feature, which can be used to further assist the modelers to improve the existing RANS models [2].

Wang et al. [2] used a group of hand-crafted ten features q_i based on the RANS simulated mean flow fields (velocity \bar{u}_i and pressure \bar{p}) as inputs \mathbf{q} to the regression function. In a more recent work [29], additional 47 mean flow features were constructed as the invariant set $\{\mathbf{S}, \mathbf{\Omega}, \nabla p, \nabla k\}$, where \mathbf{S} denotes the strain-rate tensor, $\mathbf{\Omega}$ the rotation-rate tensor, ∇p the pressure gradient and ∇k the gradient of turbulent kinetic energy, all of which are obtained from RANS-simulated mean flow fields.

Wang et al. [2] used a physics-based perturbation via the following decomposition to represent the Reynolds stress perturbations $\Delta\mathbf{R}$ [11,14]:

$$\mathbf{R} = 2k \left(\frac{\mathbf{I}}{3} + \mathbf{A} \right) = 2k \left(\frac{\mathbf{I}}{3} + \mathbf{V} \mathbf{\Lambda} \mathbf{V}^T \right) \tag{5}$$

where k is the turbulent kinetic energy, which indicates the magnitude of \mathbf{R} ; \mathbf{I} is the second order identity tensor; \mathbf{A} is the anisotropy tensor; $\mathbf{\Lambda} = \text{diag}[\lambda_1, \lambda_2, \lambda_3]$ and $\mathbf{V} = [\mathbf{v}_1, \mathbf{v}_2, \mathbf{v}_3]$ are the eigenvalues and orthonormal eigenvectors of \mathbf{A} , representing its shape (i.e., aspect ratio) and orientation, respectively. The eigenvectors \mathbf{V} consist of three orthonormal vectors (nine elements in total) but have only three degrees of freedom.

Therefore, if we visualize the Reynolds stress as an ellipsoid [30], the discrepancy between the modeled Reynolds stress \mathbf{R} and the corresponding true \mathbf{R}^* can be formulated as three consecutive transformations (i.e., perturbations):

1. The size of the ellipsoid (magnitude of the tensor) is scaled by a positive factor of $\gamma_k = k^*/k^{rans}$ while keeping the shape the same, as illustrated in Fig. 1(a).
2. The aspect ratio of ellipsoid is perturbed while keeping the size (sum of the three axes) and orientation unchanged. This is achieved by perturbing the eigenvalues, i.e., $\mathbf{\Lambda}^* = \mathbf{\Lambda} + \Delta\mathbf{\Lambda}$, as illustrated in Fig. 1(b).
3. Finally, the ellipsoid experiences a rigid-body rotation, which is represented as $\mathbf{V}^* = \mathbf{Q}\mathbf{V}$, where \mathbf{Q} is a rotation matrix. This perturbation is illustrated in Fig. 1(c).

The objective of the machine learning is to predict the mapping $f : \mathbf{q} \mapsto (\gamma, \Delta\mathbf{\Lambda}, \mathbf{Q})$, with which the corrected Reynolds stress \mathbf{R}^* can be recovered as follows:

$$\mathbf{R}^* = 2k^* \left(\frac{\mathbf{I}}{3} + \mathbf{V}^* \mathbf{\Lambda}^* \mathbf{V}^{*T} \right) = 2\gamma_k k \left(\frac{\mathbf{I}}{3} + \mathbf{Q}\mathbf{V}(\mathbf{\Lambda} + \Delta\mathbf{\Lambda})\mathbf{V}^T \mathbf{Q}^T \right). \tag{6}$$

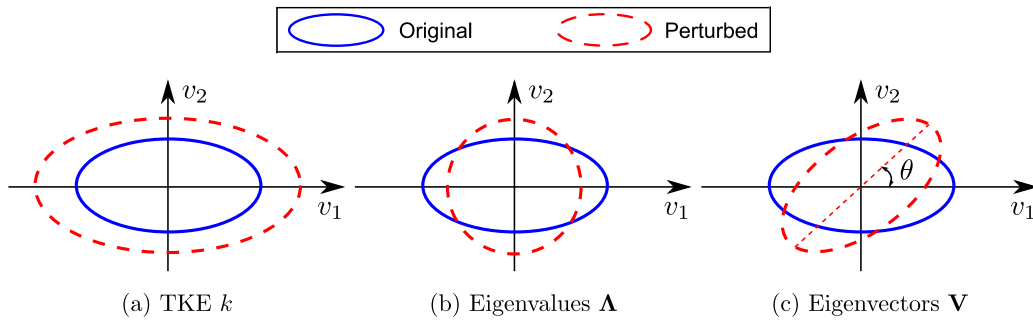


Fig. 1. The perturbations on (a) the magnitude (turbulent kinetic energy k), (b) eigenvalues Λ , and (c) eigenvectors \mathbf{V} of a Reynolds stress tensor \mathbf{R} . For clarity, the tensor is represented in the two-dimensional space as an ellipsis instead of a three-dimensional ellipsoid. In addition, perturbations on k , Λ , and \mathbf{V} are shown individually on each panel and not as three consecutive perturbations.

With perturbations of the magnitude, the shape and the orientation as introduced above, the perturbations to the Reynolds stress tensor are parameterized by six independent variables, which account for the six degrees of freedom of a symmetric second-order tensor. Noted that the perturbations can be alternatively introduced through the coefficients in the general form of eddy viscosity model [31], which has ten coefficients and introduces redundancy. This approach has been explored by Ling et al. [32]. In contrast, the scheme we adopt here is free from such redundancy in the parameterization. That is, different perturbations are guaranteed to result in different perturbed Reynolds stresses. The perturbation on the magnitude is parameterized by the logarithmic discrepancy $\log_2(k^*/k^{rans})$ [2]. The perturbations on the eigenvalues are parameterized by the Barycentric coordinates [11,14], which ensure the realizability of the perturbed Reynolds stresses. See Ref. [2] for more details. While representing the perturbations on the magnitude and the shape is straightforward, the rotation can be difficult to represent. Several schemes are introduced and examined below.

3. Representing rigid-body rotation of eigenvectors in machine learning

It has been established above that representing eigenvector perturbations as rigid-body rotations ensures orthonormality of the obtained eigenvectors and realizability of the perturbed Reynolds stresses. An apparently straightforward representation of such a rotation is to use the matrix \mathbf{Q} . However, it has nine elements (i.e., direction cosines) but only three intrinsic degrees of freedom due to the orthonormality constraint $\mathbf{Q}^T\mathbf{Q} = \mathbf{I}$. Existing machine learning algorithms are not suitable for learning quantities with hard constraints, since they were developed mostly for commercial applications (e.g., product preferences of customers), where hard constraints are uncommon. Building constraints into the learning problem is not trivial. Hence, it is more desirable to use a formulation with the same number of *independent* variables as the number of intrinsic degrees of freedom. Two candidate representations, Euler angles and unit quaternion, are introduced and compared in the context of machine learning.

Before presenting the two representations, we shall first put forward two desirable properties of the regression function $f : \mathbf{q} \mapsto \Delta\mathbf{R}$ to be learned from training data. First, the function must be smooth for it to have good generalization performance, i.e., the predictive performance of the trained function on data unseen during the training. The word “smooth” shall be interpreted in liberal sense (i.e., the output $\Delta\mathbf{R}$ varies mildly in the feature \mathbf{q} space) rather than in a mathematical sense (i.e., the existence of arbitrarily high order derivatives). The reason for such a requirement is that non-smooth functions are more susceptible to overfitting caused by the noises in the training data, which would in turn diminish the predictive capabilities of the trained functions [27]. Second, the regression function itself must be frame-independent. This is a requirement unique for constitutive modeling in computational mechanics (including turbulence modeling) [see e.g., 7,31], which is equally applicable to theory-based modeling and data-driven modeling.

For flows considered in this work (incompressible flows free from any geometric discontinuities), the mean flow features \mathbf{q} are smooth spatially. Moreover, all chosen features are frame-independent. Consequently, the two requirements outlined above on f translate to those on the output $\Delta\mathbf{R}$, i.e., it should be spatially smooth and frame-independent. Note that it is possible that both the input and the output (e.g., \mathbf{q} and $\Delta\mathbf{R}$) are frame-dependent but the mapping f is frame-independent, which is common in many analytical constitutive relations. We use the linear eddy

viscosity model $\text{dev}(\mathbf{R}) = 2\nu_t\mathbf{S}$ to illustrate this subtle point, where ν_t is a scalar eddy viscosity field. Here, both \mathbf{R} and \mathbf{S} are frame-dependent, but the mapping itself is frame-independent. However, if this function is to be learned from data, the training data need to be duplicated in a large number of rotated frames so that the machine learning algorithm can discover the uniqueness of that function in all these frames, which dramatically increases computational costs. Therefore, it is preferable to use the invariants of the tensors of concern (\mathbf{S} and \mathbf{R}) as inputs and outputs instead [33]. This is a unique complication in machine-learning-based modeling that is not present in traditional, theory-based modeling.

3.1. Euler angles

The Euler angles used in this work follows the $z-x'-z''$ convention in rigid body dynamics [34]. That is, if a local coordinate system $x-y-z$ spanned by the three eigenvectors was initially aligned with the global coordinate system ($X-Y-Z$), the current configuration could be obtained by the following three consecutive intrinsic rotations about the axes of the local coordinate system: (1) a rotation about the z axis by angle ϕ_1 , (2) a rotation about the x axis by ϕ_2 , and (3) another rotation about its z axis by ϕ_3 . In general the local coordinate axes change orientations after each rotation. Such a convention provides a set of Euler angles (ϕ_1, ϕ_2, ϕ_3) to describe the current orientation of a rigid body (or eigenvectors \mathbf{V} in this case) within a global coordinate system. We refer to this description as “absolute Euler angles”. With this description, the discrepancy between two sets of eigenvectors, \mathbf{V} and \mathbf{V}^* , can be described by the discrepancies $\Delta\phi_\alpha$ in their absolute Euler angles, ϕ_α and ϕ_α^* , respectively, with $\Delta\phi_\alpha = \phi_\alpha^* - \phi_\alpha$ and $\alpha = 1, 2, 3$. In the machine-learning-assisted turbulence modeling framework of Wang et al. [2], regression functions for $\Delta\phi_\alpha$ were trained by using high-fidelity data. However, it can be seen that this representation relies on a global coordinate system, which makes it frame-dependent. In particular, it is inadequate for more complex scenarios and can lead to deteriorated predictive performances. The importance of frame-independence in machine-learning-assisted physical modeling has been discussed in [33]. A possible remedy of the frame dependence in the formulation above is to directly describe the rotation from \mathbf{V} to \mathbf{V}^* in Euler angles $\phi_\alpha^{o \rightarrow *}$, where o and $*$ in the superscript indicate original and corrected, respectively. However, as will be shown by the *a priori* test in Section 4.2, the direct-rotation-based Euler angles $\phi_\alpha^{o \rightarrow *}$ are non-smooth spatially and thus undesirable in light of the smoothness requirement explained above.

In summary, the two variants of Euler-angle-based representations of the perturbation from \mathbf{V} to \mathbf{V}^* , i.e., discrepancy-based representation $\Delta\phi_\alpha$ and direct-rotation-based representation $\phi_\alpha^{o \rightarrow *}$, are plagued by their own weaknesses, namely the frame-independence and non-smoothness, respectively. These difficulties prompted us to explore the unit quaternion as an alternative representation.

3.2. Unit quaternion

Given two sets of orthonormal eigenvectors \mathbf{V} and \mathbf{V}^* sharing the same origin O , the Euler’s rotation theorem states there exists a unique axis of unit vector $\mathbf{n} \equiv [n_1, n_2, n_3]$ and an angle θ such that \mathbf{V}^* can be obtained via rotating \mathbf{V} by θ about an axis \mathbf{n} that runs through the origin O . The rotation can thus be represented compactly with a unit quaternion:

$$\mathbf{h} = \left[\cos \frac{\theta}{2}, n_1 \sin \frac{\theta}{2}, n_2 \sin \frac{\theta}{2}, n_3 \sin \frac{\theta}{2} \right]^T \tag{7}$$

which clearly verifies $\|\mathbf{h}\| = 1$, with $\|\cdot\|$ indicating Euclidean-norm. The axis \mathbf{n} and the angle θ are both determined by \mathbf{V} and \mathbf{V}^* and do not depend on a global coordinate system. Therefore, the unit-quaternion-based representation of the rotation is frame-independent.

To conclude this section, we point out that any rotation that transforms \mathbf{V} to \mathbf{V}^* can be uniquely represented by any of the following:

- (i) a rotation matrix \mathbf{Q} ;
- (ii) a unique set of Euler angles $(\Delta\phi_1, \Delta\phi_2, \Delta\phi_3)$ or $(\phi_1^{o \rightarrow *}, \phi_2^{o \rightarrow *}, \phi_3^{o \rightarrow *})$ based on discrepancy or direct rotation, respectively; and
- (iii) a unit quaternion \mathbf{h} .

A rare exception is the scenarios involving gimbal lock for the Euler angles [35].

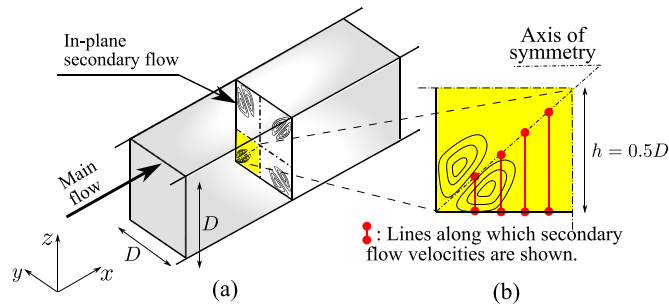


Fig. 2. Computational domain for the flow in a square duct. The x coordinate represents the streamwise direction. Secondary flows induced by Reynolds stress imbalance exist in the y - z plane as shown in panel (a). Panel (b) shows that the computational domain covers a quarter of the cross-section of the physical domain.

4. Numerical results

Numerical examples are used to evaluate the performances of three representations of perturbations to Reynolds stress eigenvectors, i.e., (1) direct-rotation-based Euler angles, (2) discrepancy-based Euler angles, and (3) unit quaternion. In the *a priori* tests, we compute the “true” perturbations that are needed to correct the RANS modeled Reynolds stress to the DNS results by using these three representations. The smoothness of such true perturbation fields is indicative of the difficulties when using data to learn the regression functions for the perturbations. The tests show that latter two representations (discrepancy-based Euler angles and unit quaternion) satisfy the smoothness requirement. Therefore, in *aposteriori* tests we focus on these two representations. Predictive performances of the machine-learning models with the latter two representations are assessed by investigating several training-prediction scenarios. The results suggest that the unit quaternion representation leads to better results due to its frame-independence. This advantage is particularly clear when the training and test flows involve different coordinate systems or geometries. In *aposteriori* tests, random forest regression [36] is used to build mappings from the 50 inputs (mean flow features \mathbf{q}) in [21] to the Reynolds stress discrepancies. The number features at each split are set to 7 ($\approx \sqrt{50}$) based on the recommendation in the literature [36]. The number of trees is 300, chosen by observing the out-of-bag (OOB) errors to avoid overfitting. More details about using random forest regression to assist RANS modeling can be found in Refs. [2,21] with example codes available on the senior author’s GitHub site [37].

4.1. Simulation setup

In this work, two test cases are employed to compare the performances of three representations of eigenvectors perturbations on Reynolds stress eigenvectors. The first test case is fully developed turbulent flow in a square duct. It is well known that RANS models have difficulty in predicting the secondary flow induced by Reynolds stress imbalances [38]. A schematic is presented in Fig. 2 to show the physical domain and the computational domain. A two-dimensional simulation is performed, since the flow is fully developed along the stream-wise direction. In addition, the computational domain only covers a quarter of the cross-section as shown in Fig. 2(b) due to the symmetry of the flow along y and z directions. All lengths are normalized by the height of the computational domain $h = 0.5D$, where D is the height of the duct. The Reynolds number Re is based on the height of the computational domain h and bulk velocity U_b .

The RANS simulations are performed in an open-source CFD platform OpenFOAM, using a built-in steady-state incompressible flow solver `simpleFoam` [39], in which the SIMPLE algorithm [40] is used. Launder–Gibson Reynolds stress transport model [41] is used for the RANS simulations of both the training flow and the test flow. In the RANS simulations, the y^+ of the first cell center is kept less than 1 and thus no wall model is applied. DNS data of the training flows are obtained from Pinelli et al. [42].

Another training-prediction scenario consists of the flows over periodic hills as shown in Fig. 3. The test flow is the flow over periodic hills at $Re = 5600$. The geometry of the computational domain of the test flow is shown in Fig. 3. Compared to the test flow, the training flow is at the same Reynolds number but with a steeper hill profile as shown in Fig. 3 indicated by the dashed line. The Reynolds number Re is based on the crest height H and the

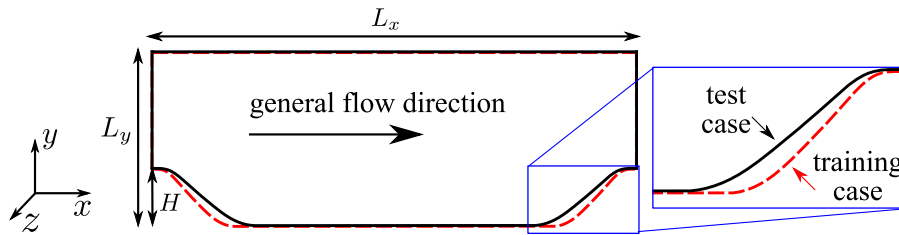


Fig. 3. Computational domain for the flow over periodic hills. The solid line indicates the configuration of the test flow. A zoom-in view shows the comparison between the hill profiles of the training flow (dashed line) and the test flow (solid line). The hill width of the training flow is 0.8 of the hill width of the test flow. The x , y and z coordinates are aligned with streamwise, wall-normal, and spanwise, respectively.

Table 1
The training-prediction scenarios in a *posteriori* test.

Cases	Training set	Test set
1	Flow in a square duct at $Re = 2900$ [42]	Flow in a square duct at $Re = 3500$ [42]
2	Flow in a square duct at $Re = 2900$ (coordinate system rotated anti-clockwise by 60°)	Flow in a square duct at $Re = 3500$ [42]
3	Flow over periodic hills at $Re = 5600$ (steeper hill profile)	Flow over periodic hills at $Re = 5600$ [47]

bulk velocity U_b at the crest. Periodic boundary conditions are applied in the streamwise (x) direction, and non-slip boundary conditions are applied at the walls. Both the DNS simulations of the training flow and the test flow are performed by using Incompact3d [43]. In Incompact3d, the incompressible Navier–Stokes equations are solved on a Cartesian mesh using sixth-order finite-difference compact schemes for the spatial discretization and a third-order Adams–Bashforth scheme for the time advancement. More details about the numerical methods used in Incompact3d can be found in [44]. A validation of our DNS results of velocity field and Reynolds stress components of the test flow show a good agreement with the results in literature [45]. All the baseline RANS simulations used Launder–Sharma $k-\epsilon$ model [46]. The y^+ of the first cell center is kept below 1, and thus no wall model is applied.

The *a priori* results are first studied to compare different metrics in this work without introducing machine learning. In the *a posteriori* results, the prediction error due to machine learning would be negligible if the same training and test data sets are used, and thus the results of this ideal situation are omitted. All the training-prediction scenarios in the *a posteriori* tests are summarized in Table 1. Scenario 1 is used to show the ideal scenario where the prediction performances based on discrepancy-based Euler angles and unit quaternion are comparable. Scenarios 2 and 3 are chosen to demonstrate the potential insufficiency of using discrepancy-based Euler angles in complex flow problems. It should be noted that the predictive capability of the machine-learning-based turbulence model is not the main focus of this work. Rather, the purpose of this paper is to illustrate the importance of embedding objectivity (frame-independence) in machine-learning-based physical modeling. Therefore, the similar training flow and test flow are intentionally chosen to make sure that the prediction error due to the difference between the training and test flows is small compared with the prediction error due to the inadequacy of discrepancy-based Euler angles with regard to frame-independence. On the other hand, the predictive capability of the machine-learning-assisted model was comprehensively investigated in [22], where different flows with massive separation were used as training flow and the prediction performance was evaluated. Two statistical metrics were also proposed in [22] to assess the prediction performance *a priori* by quantifying the difference of the training flow and the flow to be predicted.

4.2. Euler angles

In this *apriori* test, we first demonstrate that the discrepancy-based Euler angles are spatially smooth, while the direct-rotation-based Euler angles are not. It can be seen in Fig. 4(a)–(c) that the direct-rotation-based Euler angles lack the smoothness, particularly for the angles $\phi_1^{\sigma \rightarrow *}$ and $\phi_3^{\sigma \rightarrow *}$. Such lack of smoothness of Euler angles $\phi_1^{\sigma \rightarrow *}$ and $\phi_3^{\sigma \rightarrow *}$ can be explained by the rotation matrix \mathbf{Q} . Specifically, the angles $\phi_1^{\sigma \rightarrow *}$ and $\phi_3^{\sigma \rightarrow *}$ are determined by the ratio between off-diagonal terms of the rotation matrix \mathbf{Q} . In the scenario that the two eigenvectors systems are close to each other, it is expected that the rotation matrix \mathbf{Q} would be diagonal dominant, and the off-diagonal terms should

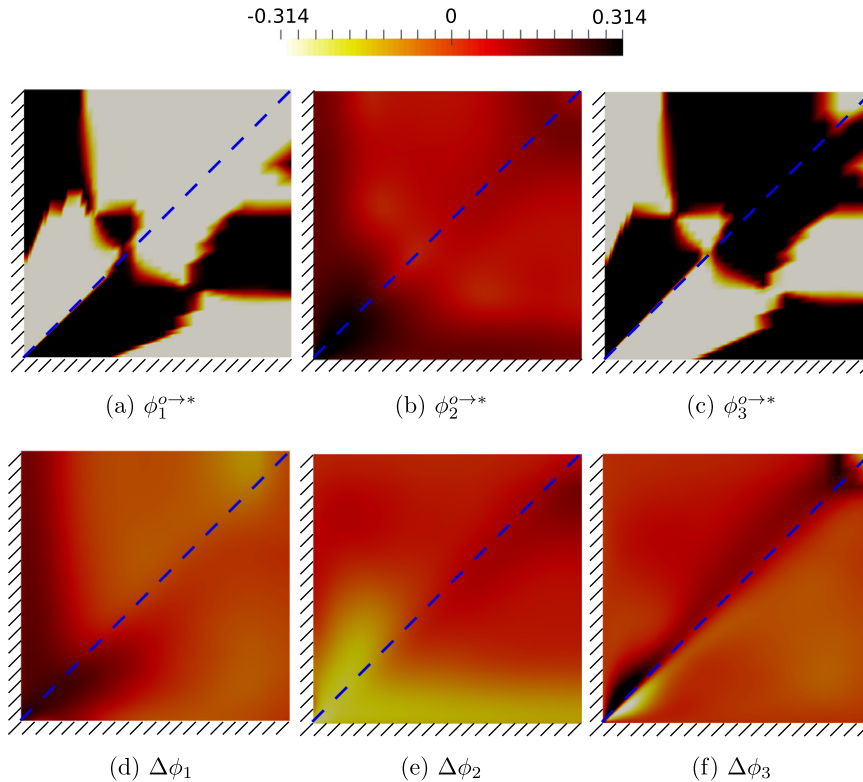


Fig. 4. Desired perturbations between the eigenvectors of the RANS modeled Reynolds stress and that of the DNS data, represented by direct-rotation-based Euler angles $\phi_\alpha^{o \to *}$ (top row) and discrepancy-based Euler angles $\Delta\phi_\alpha$ (bottom row). The dashed line denotes the diagonal of the square duct.

be small. However, the ratio between the off-diagonal terms is not necessarily small, and such ratio would be more sensitive to the change of off-diagonal Reynolds stress components. It explains the lack of smoothness for values of $\phi_1^{o \to *}$ and $\phi_3^{o \to *}$. On the other hand, it can be seen from Fig. 4(d)–(f) that the discrepancy-based Euler angles are smoother than the original Euler angles. The main reason is that the discrepancy-based Euler angles are obtained based on the difference between two sets of direct-rotation-based Euler angles, i.e., one set from RANS modeled Reynolds stress and the other from DNS data, with respect to the same global reference frame. Thus, the effect of sensitivity issue due to the small off-diagonal components of Reynolds stress tends to be canceled out, and better spatial smoothness is achieved.

The spatial smoothness can also be achieved in most regions as shown in Fig. 5 by using unit quaternion to represent the eigenvectors perturbations. The volume-averaged magnitude of gradient $J(f)$ is defined in Eq. (8) to quantitatively compare the spatial smoothness for different representations of the eigenvectors perturbations:

$$J(f) = \frac{1}{V} \int_{\mathcal{V}} \|\nabla f\| dv \quad (8)$$

where V denotes the volume of the computational domain \mathcal{V} . As shown in Table 2, the direct-rotation-based Euler angles are much rougher across the whole domain than the other two schemes. Among the three, the unit quaternion achieved the best spatial smoothness based on the integral measure J . Noted that the spatial smoothness is not achieved in Fig. 5(b) near the diagonal of square duct, as indicated by dashed line. However, there are mean flow features within the invariant set of $\{\mathbf{S}, \boldsymbol{\Omega}, \nabla p, \nabla k\}$ with the similar antisymmetric pattern. Therefore, the smoothness of the functional form $f : \mathbf{q} \mapsto \Delta \mathbf{R}$ can still be guaranteed. In addition, all the four components of unit quaternion show either symmetric or anti-symmetric pattern along the diagonal of the square duct denoted by the dashed line, indicating that these four components are invariants under the rotation of reference frame. It demonstrates the main advantage

Table 2

Volume-averaged magnitude of gradient J as defined in Eq. (8), showing the comparison of the smoothness obtained by using three representations of the eigenvectors perturbations to the Reynolds stress tensor: direct-rotation-based Euler angle, discrepancy-based Euler angle, and unit quaternion. Symbol i denotes the index of each component.

Scheme	$i = 1$	$i = 2$	$i = 3$
Direct-rotation-based Euler angle, $J(\phi_i^{o \rightarrow *})$	8.63	0.45	8.40
Discrepancy-based Euler angle, $J(\Delta\phi_i)$	0.46	0.47	0.93
Unit quaternion, $J(h_i)$	0.01	0.24	0.26

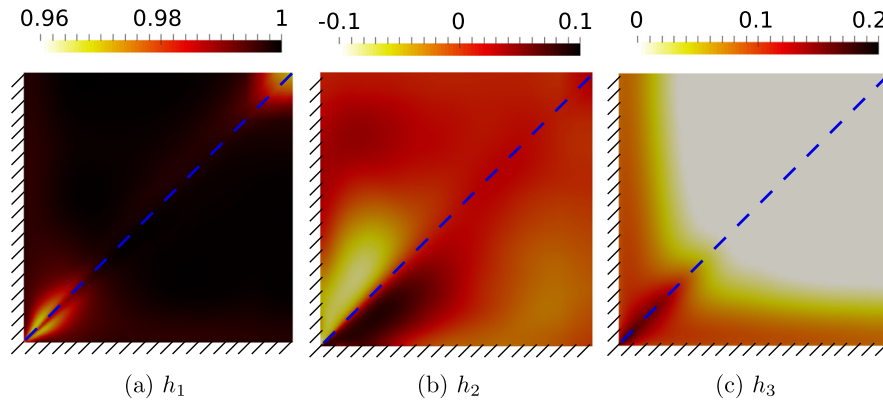


Fig. 5. The desired perturbation between the eigenvectors of the RANS modeled Reynolds stress and that of the DNS data, represented by unit quaternion \mathbf{h} . The component h_4 is omitted here since it can be expressed in terms of h_1 , h_2 , and h_3 . The dashed line denotes the diagonal of the square duct.

of unit quaternion compared to the discrepancy-based Euler angles shown in the bottom row of Fig. 4. More detailed comparisons between these two representations are presented in the *a posteriori* tests below.

4.3. *A posteriori* results

In the posteriori tests, we investigate three training-prediction scenarios to demonstrate the merit of unit quaternion by comparing the machine learning performances of discrepancy-based Euler angles and the unit quaternion.

4.3.1. Discrepancy-based Euler angles

In the first scenario, the flow in a square duct at $Re = 3500$ is predicted by using the flow at a lower Reynolds number $Re = 2900$ as the training case. We first present the prediction of discrepancy-based Euler angles in Fig. 6. It can be seen that the machine-learning-predicted discrepancy-based Euler angles demonstrate good agreements with the desired discrepancy-based Euler angles that perturb the eigenvectors of RANS modeled Reynolds stress to that of DNS data. The predictions of the desired perturbations of the eigenvalues and the turbulent kinetic energy (TKE) achieve the similar quality and thus are omitted here, considering that this work focuses on the perturbations of the eigenvectors.

The reconstructed Reynolds stress components R_{xy} and R_{xz} based on the machine learning prediction of discrepancy-based Euler angles are shown in Fig. 7. It should be noted that the machine-learning-predicted perturbations of the eigenvalues and the TKE are also employed in reconstructing the Reynolds stress components in all the following *a posteriori* tests. As shown in Fig. 7(a), the Reynolds stress component R_{xy} is significantly overestimated by the baseline RANS simulation, especially at the near corner region. The baseline RANS modeled Reynolds stress component R_{xz} is not satisfactory either, particularly near the corner. Compared to the baseline RANS results, both the reconstructed components R_{xy} and R_{xz} show much better agreements with the DNS data. This satisfactory prediction performance demonstrates the capability of using discrepancy-based Euler angles in this specific training-prediction scenario, where the training case and the prediction case share the same geometry configuration and coordinate system.

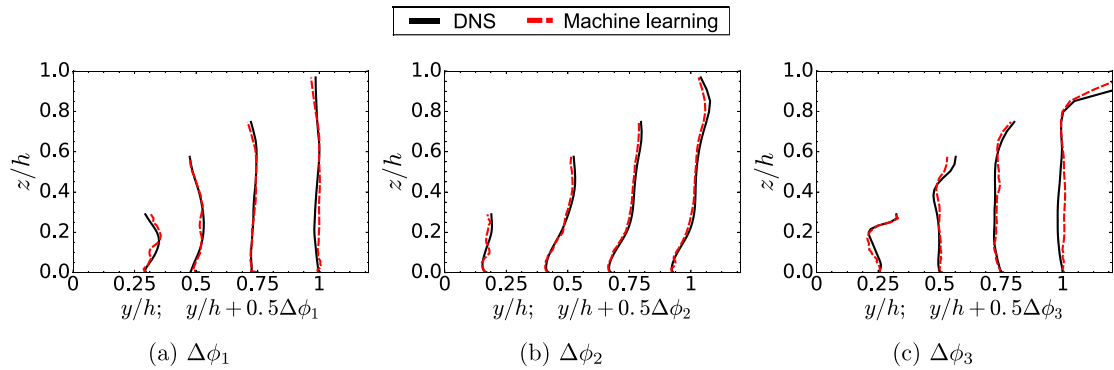


Fig. 6. The prediction of discrepancy-based Euler angles for the flow in a square duct at $Re = 3500$, showing three components: (a) $\Delta\phi_1$, (b) $\Delta\phi_2$ and (c) $\Delta\phi_3$. The training flow is the flow in a square duct at $Re = 2900$.

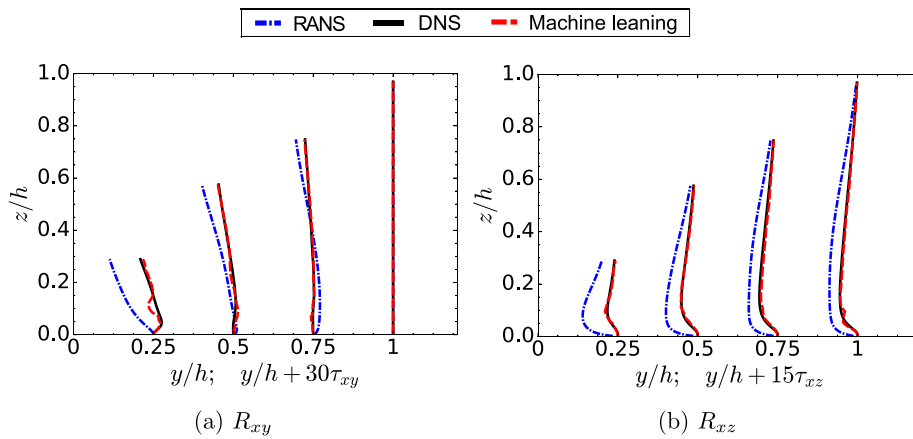


Fig. 7. The prediction of Reynolds stress components (a) R_{xy} and (b) R_{xz} based on discrepancy-based Euler angles for the flow in a square duct at $Re = 3500$. The training flow is the flow in a square duct at $Re = 2900$.

The second training-prediction scenario is chosen to demonstrate the shortcoming of the discrepancy-based Euler angles. The training flow and the test flow are the same as the first training-prediction scenario, while the coordinate system is rotated anti-clockwise by 60° for the training flow. The coordinate system of the test flow remains unchanged. The objective of this training-prediction scenario is to mimic the possible situation in complex flows in industrial applications, where the training flow and the test flow locally share the similar flow physics but different flow directions or orientations. In this situation, it is unlikely that a choice of global coordinate system is able to take into account the difference between local flow directions, and thus the coordinate system relative to the flow direction would be different for the training flow and the test flow. The prediction of discrepancy-based Euler angles for the flow in a square duct at $Re = 3500$ is shown in Fig. 8. Compared to the prediction performance as shown in Fig. 6, the predicted discrepancy-based Euler angles in Fig. 8 are less satisfactory when different coordinate systems are applied to the training flow and the test flow. Specifically, the deterioration of Euler angles is more pronounced for $\Delta\phi_1$ and $\Delta\phi_2$. This is because the discrepancy-based Euler angles are not invariants under the rotation of the reference frame.

The frame-dependence of discrepancy-based Euler angles is further demonstrated in Fig. 9 by comparing the contours of discrepancy-based Euler angles based on the original reference frame and the rotated reference frame. Since the machine learning prediction error is negligible by testing on the training data, the results in Fig. 9 can also be seen as *a posteriori* results on the training data. It can be seen that discrepancy-based Euler angle $\Delta\phi_1$ changes with the rotation of the reference frame. Another component of the discrepancy-based Euler angles $\Delta\phi_2$ also changes with the rotation of the reference frame and is omitted here for brevity. The change of discrepancy-based Euler angles of training flow would lead to a different trained regression function, since the inputs mean flow features are all invariants

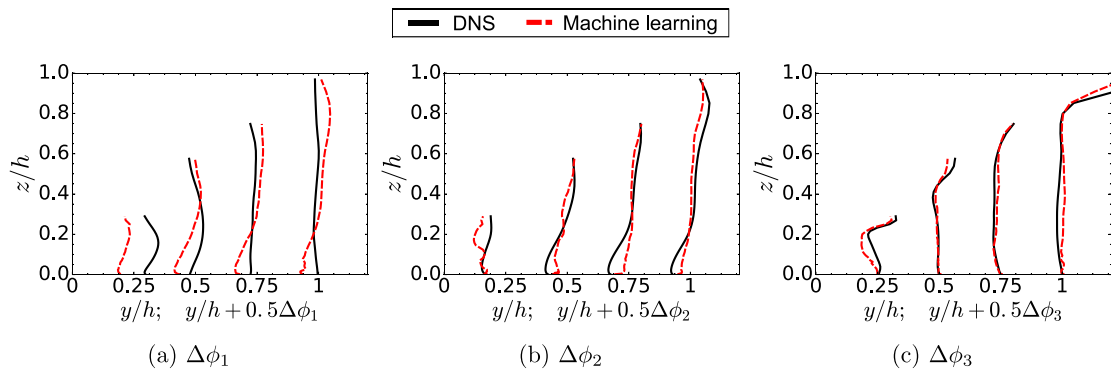


Fig. 8. The prediction of discrepancy-based Euler angles $\Delta\phi_\alpha$ for the flow in a square duct at $Re = 3500$. The training flow is the flow in a square duct at $Re = 2900$ with the coordinate system rotated by 60° .

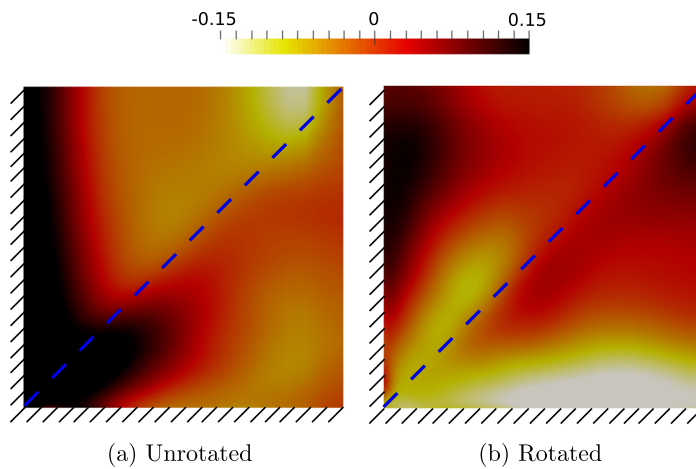


Fig. 9. The discrepancy-based Euler angles $\Delta\phi_1$ between the RANS simulated Reynolds stress and the DNS data of the training flow in a square duct at $Re = 2900$. Panel (a) corresponds to the $\Delta\phi_1$ based on the original reference frame, for which the y and z axes align with the sidewall. Panel (b) corresponds to the $\Delta\phi_1$ based on the reference frame rotated by 60° anti-clockwise. The dashed line denotes the diagonal of the square duct.

under the rotation of reference frame [48]. The frame-dependent nature of the discrepancy-based Euler angles explains the less satisfactory prediction performance as shown in Fig. 8. It demonstrates that the discrepancy-based Euler angles can potentially lead to poor prediction performance in the machine-learning-assisted turbulence modeling.

The reconstructed Reynolds stress components R_{xy} and R_{xz} based on the prediction of discrepancy-based Euler angles are shown in Fig. 10 for the second training-prediction scenario. Compared to the reconstructed Reynolds stress as shown in Fig. 7, the Reynolds stress components R_{xy} and R_{xz} show less satisfactory prediction performance. In the near-wall region, the prediction of the shear component R_{xy} is even worse than the baseline RANS simulated results. It demonstrates that the reconstructed Reynolds stress via machine-learning-predicted discrepancy-based Euler angles is potentially unreliable, even for the scenario where training flow and test flow share similar flow physics and only differ by Reynolds number (a relatively easy case for machine learning).

4.3.2. Unit quaternion

In the first training-prediction scenario, we also tested the use of the unit quaternion representation. The results of unit quaternion are shown in Fig. 11. It can be seen that the prediction performance of unit quaternion is similar to the prediction performance of discrepancy-based Euler angles as shown in Fig. 6. It is because the same geometry configuration and coordinate system are applied to both the training flow and the test flow. Thus, the frame-dependence

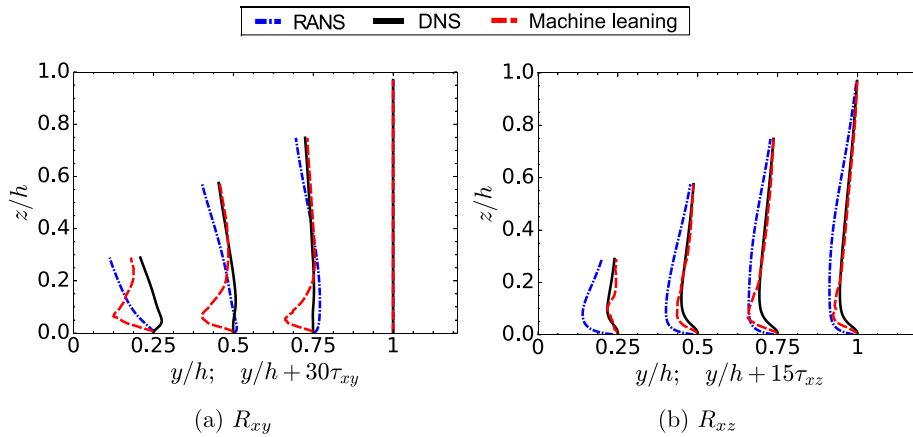


Fig. 10. The prediction of Reynolds stress components based on *discrepancy-based Euler angles* for the flow in a square duct at $Re = 3500$. The training flow is the flow in a square duct at $Re = 2900$ with the reference frame rotated by 60° anti-clockwise.

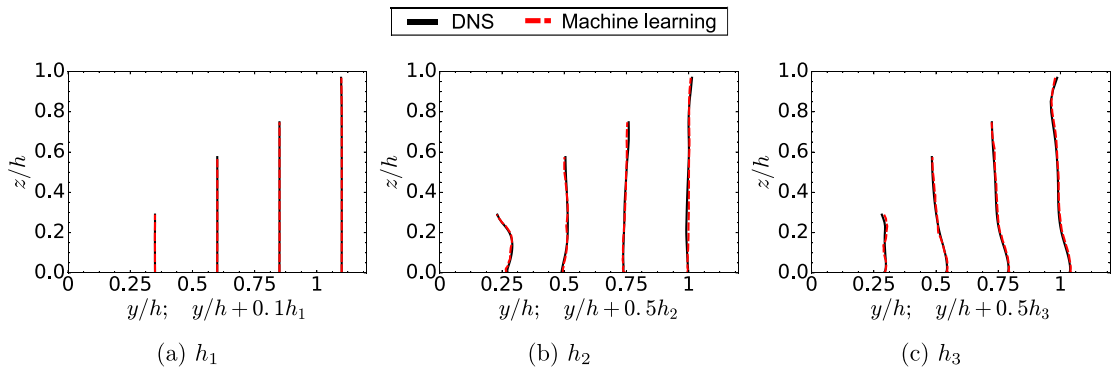


Fig. 11. The prediction of the components of unit quaternion for the flow in a square duct at $Re = 3500$. The training flow is the flow in a square duct at $Re = 2900$. The component h_4 is omitted here since unit quaternion only has three degrees of freedom.

of discrepancy-based Euler angles would not introduce additional errors into the machine learning prediction in this training-prediction scenario, explaining the similar prediction performance based on discrepancy-based Euler angles and unit quaternion.

The reconstructed Reynolds stress components R_{xy} and R_{xz} based on the prediction of unit quaternion also show satisfactory performance in Fig. 12. Such satisfactory prediction performance is comparable to the reconstructed Reynolds stress based on the prediction of discrepancy-based Euler angles shown in Fig. 7. It confirms that the similar prediction performance can be achieved for Reynolds stress components based on either discrepancy-based Euler angles or unit quaternion in this ideal training-prediction scenario. It should be noted that the unit quaternion is invariant under the change of reference frame, and thus the results based on unit quaternion for the second training-prediction scenario as listed in Table 1 would be the same as the results shown in Figs. 11 and 12.

By investigating the third training-prediction scenario, we demonstrate the merit of unit quaternion representation in a more realistic application where training flow and test flow have different geometry configurations. Before comparing the results of Euler angles and unit quaternion, we first show the prediction performance of Reynolds stress anisotropy in Fig. 13. It can be seen that the RANS results of Reynolds stress anisotropy are significantly different from the DNS data. Specifically, the RANS predicted Reynolds stress is located along the line of plane strain due to the two dimensional assumption of RANS simulation. Unlike the RANS results, the DNS data show that the Reynolds stress anisotropy is close to the two-components axisymmetric state near the bottom wall. With the increasing distance from the wall, the Reynolds stress anisotropy tends to approach the three components isotropic state, and gradually return toward the two components state while approaching the top wall. Fig. 13 shows that the

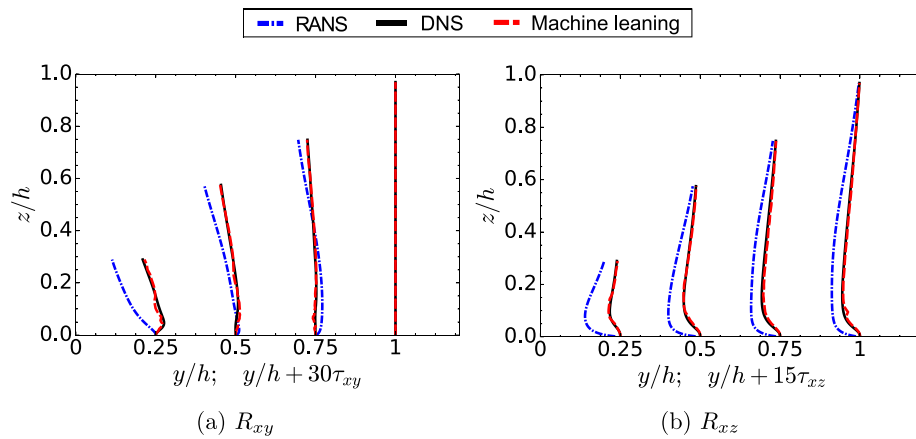


Fig. 12. The reconstructed Reynolds stress components based on the prediction of *unit quaternion* for the flow in a square duct at $Re = 3500$, including (a) shear component R_{xy} and (b) shear component R_{xz} . The training flow is the flow in a square duct at $Re = 2900$.

machine learning predicted Reynolds stress anisotropy successfully captures the trend of DNS data at several different locations. At $x/H = 3$ and $x/H = 4$, the machine learning predicted Reynolds stress anisotropy shows much better agreement with the DNS data. The reason of less satisfactory prediction at $x/H = 1$ and $x/H = 2$ is mainly due to the difference between the training flow and the test flow with regard to the steepness of the hill profile. However, it should be noted that the machine learning prediction at $x/H = 1$ and $x/H = 2$ still captures the trend of DNS data and also demonstrates quantitatively improvement than the RANS simulation results.

The desired eigenvectors perturbations for the test flow are presented in Figs. 14 and 15. It can be seen in Fig. 14 that the desired perturbations via discrepancy-based Euler angles change with the rotation of the reference frame. The comparison shown in Fig. 14 confirms this drawback resulted from the frame-dependent nature of the discrepancy-based Euler angles. The Euler axis aligns along the spanwise direction for this 2-D flow. Without rotating the original reference frame, the perturbations via discrepancy-based Euler angles only involve a single rotation and thus the discrepancy-based Euler angle $\Delta\phi_1$ should be the same as the angle θ in the unit quaternion representation. However, more complex patterns can be seen in Fig. 14 in several regions. This is because the discrepancy-based Euler angles $\Delta\phi_2$ and $\Delta\phi_3$ are not exact zeros, which can be attributed to numerical noises.

The reconstructed Reynolds stress shear component R_{xy} based on the prediction of discrepancy-based Euler angles is shown in Fig. 16(a). It can be seen that the reconstructed shear stress component R_{xy} is less satisfactory at the windward side of the hill, where the reconstructed R_{xy} is even worse than the RANS results within the near wall region. The main reason is that the different steepness of hill profiles lead to different local flow directions for the training flow and the test flow at this region. Due to the frame-dependent nature of discrepancy-based Euler angles, the trained machine-learning function from the training flow is not applicable to the test flow. Therefore, the reconstructed Reynolds stress component based on the predicted discrepancy-based Euler angles of the test flow is potentially worse than the baseline RANS results. It should be noted that the deterioration of the reconstructed shear stress component R_{xy} is less notable at the leeward of the hill, where the steepness of the hill profiles are also different for the training flow and the test flow. The main reason is that the turbulent kinetic energy is lower within the near wall region at leeward side of the hill, and thus the shifting of energy between the Reynolds stress components due to an inaccurate estimation of eigenvectors perturbation is less notable. Compared to the reconstructed Reynolds stress component in Fig. 16(a), the reconstructed R_{xy} based on the prediction of unit quaternion shows a much better agreement with the DNS data at the windward of the hill, as highlighted by a zoom-in view in Fig. 16. For the leeward side of the hill, the reconstructed R_{xy} in Fig. 16(b) is also slightly better than the one shown in Fig. 16(a). Therefore, unit quaternion provides a better representation of the eigenvectors perturbations to the Reynolds stress tensor in the context of machine-learning-assisted turbulence modeling. It can be seen that the prediction performance is less satisfactory at the leeward side in Fig. 16(a) and (b), indicating that such less satisfactory prediction is mainly due to the geometry difference between the training flow and the test flow. The main reason is that the discrepancy between DNS and RANS shear stresses of the training flow is noticeably smaller than the discrepancy of the test flow at the leeward

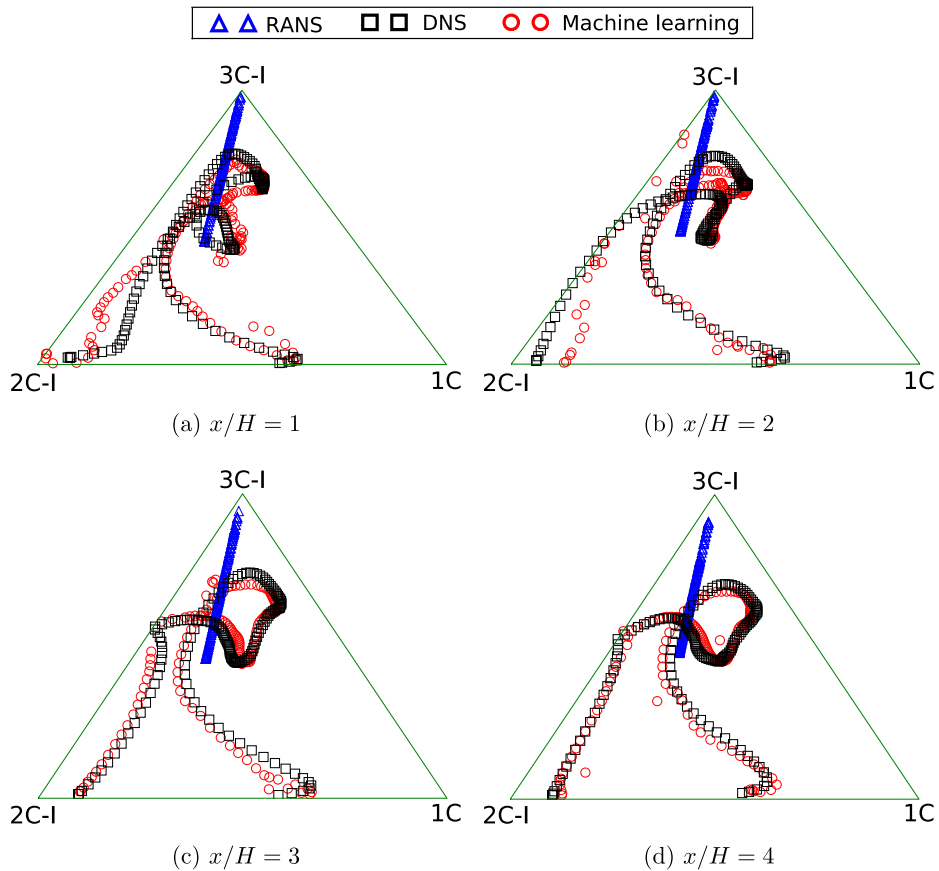


Fig. 13. The Reynolds stress anisotropy in Barycentric triangle at $x/H = 1, 2, 3$ and 4 . The three vertices of Barycentric triangle are indicated by 3C-I, 2C-I and 1C, representing the three components isotropic state, the two components axisymmetric state and the one component state, respectively. The bottom line of the Barycentric triangle denotes the two components state that corresponds to near wall turbulence due to the suppression of turbulence along the wall-normal direction.

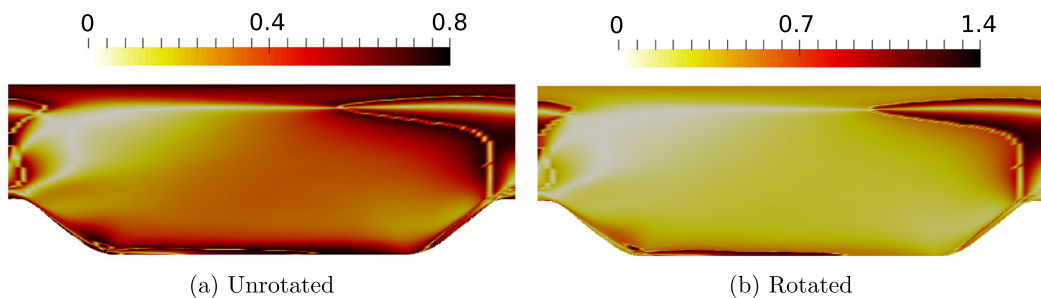


Fig. 14. The magnitude of discrepancy-based Euler angles $\Delta\phi_1$ between the RANS simulated Reynolds stress and the DNS data of the flow over periodic hills at $Re = 5600$. The results of $\Delta\phi_2$ and $\Delta\phi_3$ are omitted here since they are all close to zeros based on the unrotated reference frame. Panel (a) corresponds to the $\Delta\phi_1$ based on the original reference frame, for which the x and z axes align with the streamwise direction and the spanwise direction. Panel (b) corresponds to the $\Delta\phi_1$ based on the reference frame rotated by 60° anti-clockwise with regard to the streamwise direction.

side of the hill as shown in Fig. 17. Therefore, the machine learning model tends to underestimate the shear stress τ_{xy} around this region in Fig. 16. The prediction of shear stress at the upper boundary is also less satisfactory by using discrepancy-based Euler angles. A possible explanation of the different prediction performances near the flat

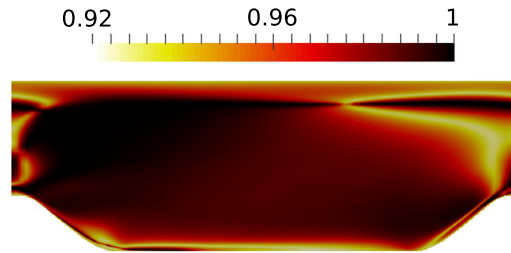


Fig. 15. The desired perturbation h_1 between the eigenvectors of the RANS modeled Reynolds stress and that of the DNS data. The components h_2, h_3 and h_4 are omitted here since the Euler axis is known to be aligned along spanwise direction for this flow.

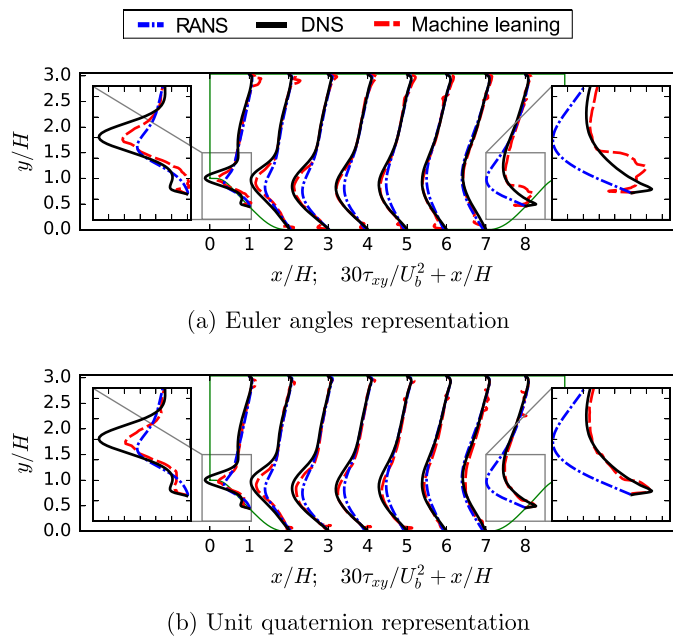


Fig. 16. The prediction of shear stress R_{xy} based on (a) discrepancy-based Euler angles and (b) unit quaternion for the flow over periodic hills at $Re = 5600$. The training flow is the flow over periodic hills at $Re = 5600$ with a steeper hill profile. A zoom-in view is added at both the windward side and the leeward side of the hill for clear comparison.

boundary layer regions is that the lower boundary and upper boundary have different complex patterns of Euler angles in Fig. 14(a), and thus the machine learning model tends to have less satisfactory prediction near the flat boundary region. In contrast, the component h_1 in Fig. 15 has a simpler pattern near the lower wall, and thus the prediction of shear stress has a better performance near the flat boundary region as shown in Fig. 16(b).

5. Conclusion

Introducing perturbations to stress tensors has important implications to model-form uncertainty estimation in RANS models and to machine-learning-assisted RANS modeling. Representing perturbations to Reynolds stress eigenvectors in the context of machine-learning-assisted modeling is challenging due to the requirements of mapping smoothness and frame-independence. In this work we formulated the eigenvector perturbations as rigid-body rotations and examined three representations: (1) the direct-rotation-based Euler angles, (2) the discrepancy-based Euler angles, and (3) the unit quaternion. A priori assessment of fully turbulent square duct flow shows that the direct-rotation-based Euler angles does not satisfy the smoothness requirement. On the other hand, the discrepancy-based Euler angle representation does not satisfy the frame-independence requirement, which has been shown theoretically and numerically with *a posteriori* tests on both the square duct flow and the flow over periodic hills. The numerical

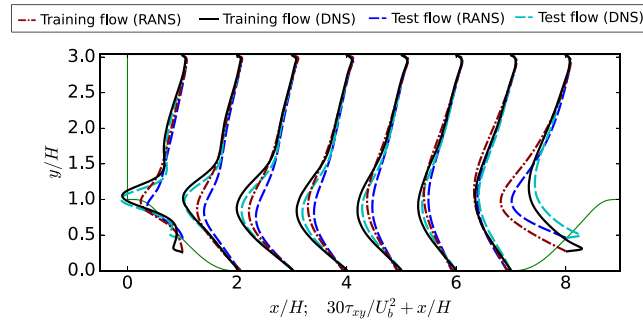


Fig. 17. The comparison of DNS and RANS data of τ_{xy} . The hill width of the training flow is 0.8 of the hill width compared with the test flow as shown in Fig. 3.

examples showed that the unit quaternion representation satisfies both requirements and is an ideal representation of Reynolds stress eigenvector perturbations. This finding has clear importance for uncertainty quantification and machine learning in turbulence modeling and for data-driven computational mechanics in general. For instance, it also has implications in other fields such as plasticity, where sequential increments of stress tensors are used to find the new stress state from the current one.

Acknowledgments

The authors would like to thank the two reviewers for their constructive and valuable comments, which helped improving the quality and clarity of this manuscript. The authors acknowledge Dr. Roney L. Thompson of Federal University of Rio de Janeiro and Dr. Jianxun Wang of University of Notre Dame for their helpful discussions during this work.

Appendix. Nomenclature

Δ	discrepancy
Λ	diagonal matrix of eigenvalues
Ω	rotation rate tensor
γ	ratio of turbulent kinetic energy
\mathbf{R}	Reynolds stress
ϕ_α	global-frame-based Euler angles
$\phi_\alpha^{\sigma \rightarrow *}$	direct-rotation-based Euler angles
\mathbf{S}	strain rate tensor
\mathbf{h}	unit quaternion
\mathbf{q}	mean flow features
\mathbf{n}	Euler axis
\mathbf{Q}	rotation matrix
\mathbf{V}	eigenvectors of second order tensor
ν_t	turbulent viscosity

References

- [1] D.C. Wilcox, *Turbulence Modeling for CFD*, third ed., DCW Industries, 2006.
- [2] J.-X. Wang, J.-L. Wu, H. Xiao, Physics-informed machine learning approach for reconstructing Reynolds stress modeling discrepancies based on DNS data, *Phys. Rev. Fluids* 2 (3) (2017) 034603.
- [3] J. Ling, A. Kurzawski, J. Templeton, Reynolds averaged turbulence modelling using deep neural networks with embedded invariance, *J. Fluid Mech.* 807 (2016) 155–166.
- [4] A.P. Singh, S. Medida, K. Duraisamy, Machine learning-augmented predictive modeling of turbulent separated flows over airfoils. arXiv preprint arXiv:1608.03990.

- [5] B. Tracey, K. Duraisamy, J.J. Alonso, A machine learning strategy to assist turbulence model development, AIAA Paper 1287 (2015) 2015.
- [6] A.P. Singh, K. Duraisamy, Using field inversion to quantify functional errors in turbulence closures, *Phys. Fluids* 28 (2016) 045110.
- [7] S.B. Pope, *Turbulent Flows*, Cambridge University Press, Cambridge, 2000.
- [8] H. Xiao, J.-L. Wu, J.-X. Wang, Physics-informed machine learning for predictive turbulence modeling: Progress and perspectives, in: 2017 AIAA SciTech Forum and Exposition, 2017, Grapevine, TX, 2017, AIAA, Reston, VA, 2017, paper 2017-1712.
- [9] R.N. King, P.E. Hamlington, W.J. Dahm, Autonomic closure for turbulence simulations, *Phys. Rev. E* 93 (3) (2016) 031301.
- [10] A. Vollant, G. Balarac, C. Corre, Subgrid-scale scalar flux modelling based on optimal estimation theory and machine-learning procedures, *J. Turbul.* (2017) 1–25.
- [11] M. Emory, J. Larsson, G. Iaccarino, Modeling of structural uncertainties in Reynolds-averaged Navier–Stokes closures, *Phys. Fluids* 25 (11) (2013) 110822.
- [12] M. Emory, R. Pecnik, G. Iaccarino, Modeling structural uncertainties in Reynolds-averaged computations of shock/boundary layer interactions, AIAA Paper 479 (2011) 1–16.
- [13] M.A. Emory, Estimating Model-Form Uncertainty in Reynolds-Averaged Navier–Stokes Closures (Ph.D. thesis), Stanford University, 2014.
- [14] S. Banerjee, R. Krahl, F. Durst, C. Zenger, Presentation of anisotropy properties of turbulence, invariants versus eigenvalue approaches, *J. Turbul.* 8 (32) (2007) 1–27.
- [15] J.L. Lumley, G.R. Newman, The return to isotropy of homogeneous turbulence, *J. Fluid Mech.* 82 (01) (1977) 161–178.
- [16] R. Thompson, L. Sampaio, W. Edeling, A.A. Mishra, G. Iaccarino, A strategy for the eigenvector perturbations of the Reynolds stress tensor in the context of uncertainty quantification, in: Proceedings of the Summer Program, Center for Turbulence Research, 2016, p. 10.
- [17] G. Iaccarino, A.A. Mishra, S. Ghili, Eigenspace perturbations for uncertainty estimation of single-point turbulence closures, *Phys. Rev. Fluids* 2 (2) (2017) 024605.
- [18] J.-X. Wang, R. Sun, H. Xiao, Quantification of uncertainties in turbulence modeling: A comparison of physics-based and random matrix theoretic approaches, *Int. J. Heat Fluid Flows* 62 (2016) 577–592.
- [19] J.-X. Wang, J.-L. Wu, J. Ling, G. Iaccarino, H. Xiao, Towards a Complete Framework of Physics-Informed Machine Learning for Predictive Turbulence Modeling, Tech. Rep., in: Proceedings of Summer Research Program, Center of Turbulence Research, Stanford University, Stanford, CA, USA, 2016.
- [20] K. Duraisamy, G. Iaccarino, H. Xiao, Turbulence modeling in the age of data, *Annu. Rev. Fluid Mech.* 51 (2019) 357–377, <http://dx.doi.org/10.1146/annurev-fluid-010518-040547>.
- [21] J.-L. Wu, H. Xiao, E. Paterson, Physics-informed machine learning approach for augmenting turbulence models: A comprehensive framework, *Phys. Rev. Fluids* 3 (7) (2018) 074602.
- [22] J.-L. Wu, J.-X. Wang, H. Xiao, J. Ling, A priori assessment of prediction confidence for data-driven turbulence modeling, *Flow Turbul. Combust.* 99 (2017) 25–46.
- [23] D.Q. Huynh, Metrics for 3d rotations: Comparison and analysis, *J. Math. Imaging Vision* 35 (2) (2009) 155–164.
- [24] J.J. Kuffner, Effective sampling and distance metrics for 3d rigid body path planning, in: 2004 IEEE International Conference on Robotics and Automation, ICRA'04, in: 2004 Proceedings, vol. 4, IEEE, 2004, pp. 3993–3998.
- [25] B.K. Horn, Closed-form solution of absolute orientation using unit quaternions, *J. Opt. Soc. Amer. A* 4 (4) (1987) 629–642.
- [26] D.J. Heeger, A. Jepson, Simple method for computing 3d motion and depth, in: Third International Conference on Computer Vision, in: 1990 Proceedings, IEEE, 1990, pp. 96–100.
- [27] P. Domingos, A few useful things to know about machine learning, *Commun. ACM* 55 (10) (2012) 78–87.
- [28] T.A. Oliver, R.D. Moser, Bayesian uncertainty quantification applied to RANS turbulence models, in: *Journal of Physics: Conference Series*, 318, IOP Publishing, 2011, 042032.
- [29] J.-X. Wang, J.-L. Wu, J. Ling, G. Iaccarino, H. Xiao, Physics-informed Machine Learning for Predictive Turbulence Modeling: Towards a Complete Framework, Tech. Rep., in: Proceedings of the Summer Program, Center of Turbulence Research, Stanford University, 2016.
- [30] A. Simonsen, P.-Å. Krogstad, Turbulent stress invariant analysis: Clarification of existing terminology, *Phys. Fluids* 17 (8) (2005) 088103.
- [31] S. Pope, A more general effective-viscosity hypothesis, *J. Fluid Mech.* 72 (02) (1975) 331–340.
- [32] J. Ling, R. Jones, J. Templeton, Machine learning strategies for systems with invariance properties, *J. Comput. Phys.* 318 (2016) 22–35.
- [33] J. Ling, R. Jones, J. Templeton, Machine learning strategies for systems with invariance properties, *J. Comput. Phys.* 318 (2016) 22–35.
- [34] H. Goldstein, The Euler angles, in: *Classical Mechanics*, 1980, pp. 143–148.
- [35] J.B. Kuipers, et al., *Quaternions and Rotation Sequences*, Vol. 66, Princeton University Press, Princeton, 1999.
- [36] L. Breiman, Random forests, *Mach. Learn.* 45 (1) (2001) 5–32.
- [37] Data-driven turbulence modeling with physics-informed machine learning, 2018. <https://github.com/xiaoh/turbulence-modeling-PIML>.
- [38] A. Huser, S. Biringen, Direct numerical simulation of turbulent flow in a square duct, *J. Fluid Mech.* 257 (1993) 65–95.
- [39] H.G. Weller, G. Tabor, H. Jasak, C. Fureby, A tensorial approach to computational continuum mechanics using object-oriented techniques, *Comput. Phys.* 12 (6) (1998) 620–631.
- [40] S. Patankar, *Numerical Heat Transfer and Fluid Flow*, CRC Press, 1980.
- [41] M. Gibson, B. Launder, Ground effects on pressure fluctuations in the atmospheric boundary layer, *J. Fluid Mech.* 86 (03) (1978) 491–511.
- [42] A. Pinelli, M. Uhlmann, A. Sekimoto, G. Kawahara, Reynolds number dependence of mean flow structure in square duct turbulence, *J. Fluid Mech.* 644 (2010) 107–122.
- [43] S. Laizet, N. Li, Incompact3d: A powerful tool to tackle turbulence problems with up to $O(10^5)$ computational cores, *Internat. J. Numer. Methods Fluids* 67 (11) (2011) 1735–1757.
- [44] S. Laizet, E. Lamballais, High-order compact schemes for incompressible flows: A simple and efficient method with quasi-spectral accuracy, *J. Comput. Phys.* 228 (16) (2009) 5989–6015.

- [45] M. Breuer, N. Peller, C. Rapp, M. Manhart, Flow over periodic hills: Numerical and experimental study in a wide range of Reynolds numbers, *Comput. & Fluids* 38 (2) (2009) 433–457.
- [46] B. Launder, B. Sharma, Application of the energy-dissipation model of turbulence to the calculation of flow near a spinning disc, *Lett. Heat Mass Transfer* 1 (2) (1974) 131–137.
- [47] M. Breuer, N. Peller, C. Rapp, M. Manhart, Flow over periodic hills—numerical and experimental study in a wide range of Reynolds numbers, *Comput. & Fluids* 38 (2) (2009) 433–457.
- [48] J. Ling, J. Templeton, Evaluation of machine learning algorithms for prediction of regions of high Reynolds averaged Navier–Stokes uncertainty, *Phys. Fluids (1994-present)* 27 (8) (2015) 085103.